



Mode I fracture of thick adhesively bonded GFRP composite joints for wind turbine rotor blades

Jialiang Fan^a, Anastasios P. Vassilopoulos^b, Veronique Michaud^{a,*}

^a Laboratory for Processing of Advanced Composites (LPAC), Institute of Materials (IMX), Ecole Polytechnique Fédérale de Lausanne (EPFL), Lausanne, Switzerland

^b Composite Construction Laboratory (CCLab), Ecole Polytechnique Fédérale de Lausanne (EPFL), Lausanne, Switzerland

ARTICLE INFO

Keywords:

Fracture

Thick bonded joints

Adhesives

Composites

ABSTRACT

This article investigates the effects of voids, joint geometry, and test conditions on the quasi-static Mode I fracture performance of thick adhesive Double Cantilever Beam (DCB) joints such as those prevailing in wind industry and shipbuilding. The specimens were made by glass fiber reinforced epoxy adherend and SikaPower®-830 epoxy adhesive in the cm thickness range. Side-grooved shape guided the crack propagation direction and assisted stable propagation, while lower cross-head displacement rates reduced the occurrence of unstable crack propagation and prevented crack deflection. Porosities, which are inevitable due to the high viscosity of the adhesive, led to unstable propagation and promoted crack path deviations. They could also decrease the apparent fracture energy release rate (SERR) since the crack surface is reduced. In conclusion, grooved DCB joints with low void content tested at low displacement rates showed stable crack propagation without significant crack path deviation. This method enables comparison with future adhesive formulations and the refinement of full-scale blade models.

1. Introduction

With the market share of wind energy keeps growing during the last several years [1], recent developments in wind energy constantly push for larger wind turbine rotor blades (WTRB) to achieve lower energy cost [2]. The large WTRBs today, reaching or exceeding 100 m in length, [3], are typically constructed by assembling several composite components with structural adhesives. The bondline thickness in these massive structures is within the cm range and varies along the length of the blades.

The failure of these thick adhesive joints was observed from post-mortem examinations and full-scale WTRB experiments, which showed that WTRBs fail usually after damage initiated and propagated in the thick adhesive joints under complex stress states [4–6]. Nonetheless, investigations of the thick adhesive joints' fracture behavior are scarce in the literature and remain limited to Mode I fracture, due to the test configuration simplicity [7–10].

Double cantilever beam tests have been widely used for the investigation of the Mode I fracture behavior of thin adhesively bonded joints with metallic and composite adherends. However, adapting the relevant standards and the experimental techniques for examining thick adhesive

joint configurations is challenging, since undesired phenomena, such as crack propagation deviation and unstable crack propagation, are observed in such tests making the investigation more complicated and the interpretation of the results for deriving meaningful fracture data doubtful.

The crack propagation path is difficult to be guided or predicted in advance in thick joints. For example, Lopes Fernandes et al. [7] investigated thick DCB joints with epoxy adhesive layers and glass fiber reinforced epoxy adherends and observed that cracks deviated rapidly from the midplane of the joint. Bautista Villamil et al. [8] also reported a similar behavior. The crack path changed from the middle plane of the adhesive layer to inside the adherend and propagated within the adherend as a mixed-mode delamination. Saleh et al. [9] fabricated thick DCB adhesive joints with about 8 mm thick epoxy adhesive layer and steel adherends. The crack growth started from the interface pre-crack, and finally propagated at the middle plane of the adhesive layer. In conclusion, stable cohesive failure within the adhesive layer without any crack deviation has not been achieved for DCB joints with thick adhesive layers.

Changing crack path is not a unique characteristic for thick adhesive joints, since similar behavior has been reported for adhesive joint

* Corresponding author.

E-mail address: veronique.michaud@epfl.ch (V. Michaud).

<https://doi.org/10.1016/j.compstruct.2023.117705>

Received 27 June 2023; Received in revised form 27 September 2023; Accepted 4 November 2023

Available online 5 November 2023

0263-8223/© 2023 The Authors. Published by Elsevier Ltd. This is an open access article under the CC BY license (<http://creativecommons.org/licenses/by/4.0/>).

experiments with thinner adhesive layers (<5mm) under Mode I, Mode II and mixed-mode conditions both in quasi-static and fatigue loading [11–14]. The initial pre-crack was located at the interface between the adhesive and adherend. To induce cracks at various layers within the adherend, the pre-crack area of the adherends was then polished to different depths. During the quasi-static and fatigue tests, the crack path was observed to change, and roving bridging was noted in quasi-static tests. As a result, the corresponding SERR curves exhibited a rising and then declining trend.

Simple beam theory (SBT), corrected beam theory (CBT), and experimental compliance method (ECM) are already used for these aforementioned pultruded composite joints [11–14]. These three methods are still applicable for thick adhesive joints, while the calculation of SBT needs to be modified to include the influence of adhesive layer on second moment of inertia. In addition, the implementation of Penado-Kanninen model was also reported for SERR calculation, where the beam was partially unsupported and partially bolstered by elastic foundation [7].

A grooved-shape design has been proposed for pure material DCB tests by Mostovoy et al. [15]. They evaluated the possibility of adding crack-directing side grooves to test bulk materials, such as metal, because during these tests, even if unstable crack propagation occurred, the crack-arrested position would remain within the grooved plane. It is also proven to be beneficial in controlling the crack propagation direction [16]. After this, many material studies were established on grooved specimens [16–19]. A similar principle has been applied to thin adhesive joints. Komatsu et al. [20] narrowed the width of epoxy adhesive layer to prevent the plastic deformation of steel adherend. However, these new geometrical configurations, such as grooved shapes, were not introduced in the past to facilitate the investigation of thick adhesive joint behavior avoiding the aforementioned crack path deviation problems.

Unstable crack propagation, also called as stick–slip crack propagation behavior [21] is another fracture behavior that needs to be considered. It is commonly observed during thin adhesive joint tests. The reason is complex, including the type of adhesive, loading rate, test environment temperature, the difference between crack initiation energy and propagation energy, as well as the presence of voids [21–24]. However, for thin adhesive joints, even though stick–slip takes place, the crack is constrained by the adherends, so the arrested position is still in the middle of the joints. The occurrence of this phenomenon can extend to joints with a thick adhesive layer, even though not found in published literature. Besides, compared with thin adhesive joints, the adherends' constraint is less pronounced within thick adhesive joints, so the arrested position is unpredictable and may deviate from the middle plane of the joints.

Previous research has established that propagation stability of thin adhesive joints is affected by loading rate, which varies with the type of adhesives. Blackman et al. [24] investigated thin epoxy adhesive joints where stick–slip crack propagation was detected within a certain range of loading rates, i.e. from 0.1 m/s to around 15 m/s. When the loading rate is smaller than 0.1 m/s or higher than 15 m/s, stable crack propagation was observed. Schmandt et al. [25] studied hyperelastic polyurethane adhesive with a J-integral method. They claimed similar results. When the cross-head velocity was smaller than 0.01 mm/s or larger than 1 mm/s, crack propagation instability tended to abate. Modifying the loading rate is an effective strategy to prevent stick–slip propagation in thin adhesive joints, and this approach may also be extended to thick adhesive joints.

Besides these well-known features shared between thin and thick adhesive joints, one significant difference is the presence of voids. Degassing and pressure are enough to eliminate most large voids for thin adhesive joints, except for joints with aluminum adherends, since voids were observed in the thin adhesive layer between aluminum adherends. This was attributed to air adsorption of the heavily deformed aluminum surfaces, which led to void formation within the adhesive layer by

diffusion [26,27]. In contrast, it is more intricate for thick adhesive joints, which are made from very viscous epoxy pastes, which exhibit a yield stress behavior for better deposition during blade assembly. Due to the size, viscosity and manufacturing process, large voids always exist within the thick adhesive layer [28,29]. Although several possible ways of avoiding large voids are proposed, such as mixing under vacuum and centrifuging the mixed adhesive, these methods still cannot eliminate all the internal voids [30,31]. Voids could lead to the decrease of bonding area and stress concentration and cause premature failure. For example, Florian et al. [32] conducted sub-component tests and concluded that a single defect is not harmful while many defects would reduce the fatigue lifetime of the component. Nevertheless, few researchers have been able to draw any conclusion from systematic research into the influence of voids. The majority of the research on this topic has been mostly restricted to the influence of a single void on the behavior of thin adhesive joints, whereas the void content influence on thick adhesive joint fracture behavior is still not well understood [33–35].

The literature review showed that the presence of voids, the loading rate, and the side grooves are parameters affecting the fracture performance of thin adhesively bonded joints. To the authors' knowledge, the impact of the side grooved shape on thick adhesive joint behavior has not been explored and the effect of loading rate on stick–slip propagation has not been examined for thick adhesive joints. The influence of the average void content is also unclear, as prior research only focused on individual voids.

This study investigates the effect of the aforementioned factors on the fracture behavior of thick adhesive joints by conducting DCB quasi-static mode I experiments and tries to identify the best experimental conditions (loading rate) and the limits of geometrical parameters (specimen geometry and grooves) and manufacturing defects (voids) aiming at guiding the crack to propagate stably within the middle plane allowing the estimation of the adhesive SERR based on the three common methods used for thin adhesive joints.

The scope of this study is constrained to the particular bonded joint, and the elucidation of the fracture behavior refers to the bonded joint specifically rather than the adhesive in isolation.

2. Materials and methods

DCB joints were made with glass fiber reinforced epoxy adherend and epoxy adhesive. The composite adherend was manufactured with vacuum assisted infusion process. Unidirectional glass fibers were supplied by GIVIDI FABRIC S.R.L. with areal weight of 430 g/m². The epoxy resin and hardener were EPIKOTE™ Resin MGS RIMR 135 and EPIKOTE™ Resin MGS RIMH 137 respectively.

The Sikapower®-830 (SP830) adhesive used for the joints was supplied by Sika technology AG. It is a two-component epoxy adhesive, intended for wind turbine blade manufacturing. The curing process for this adhesive involves heating to 70 °C for four hours, according to the datasheet. Although SP830 has adequate yield stress rheology for blade manufacturing, its high viscosity leads to joint manufacturing problems, including difficulties in controlling the thickness and the void content. Two different fabrication methods were followed in this work to avoid these problems. For the SERR calculation, elastic modulus of adherend and adhesive is required, which is determined by tensile test in accordance with ASTM standard D3039 and D638 [36,37].

2.1. Coupon tensile specimen fabrication and test method

2.1.1. Adhesive

Type I dog-bone SP830 adhesive specimens according to ASTM D638-22 [36] were manufactured within a metal mold. Sika liquid wax 815 was applied to the metal mold before manufacturing as demolding agent. After demolding, the specimen edges were polished and metal tabs were glued with Jowat® Cyanoacrylate Adhesives. A universal testing machine (Walter + Bai AG, Switzerland, 125 kN capacity)

equipped with a 10 kN load cell with $\pm 0.5\%$ accuracy and a contact extensometer with $\pm 1\ \mu\text{m}$ accuracy were used for the tensile experiments at a constant deformation rate of 2 mm/min.

2.1.2. Composite

Composite $[90/0]_S$ laminates were manufactured with vacuum infusion and cured at room temperature for 24 h and then underwent a post-curing process, which involved a low-speed temperature ramp for 2 h from 20 °C to 60 °C, followed by 9.5 h at 60 °C, and finally 6 h at 80 °C. Prismatic specimens of 25 mm * 250 mm were water-jet cut from the aforementioned laminates at 0°. Prior to testing, DIC pattern was sprayed on one side of the specimens and aluminum tabs of 25 mm * 45 mm were glued with Jowat® Cyanoacrylate Adhesives. Tensile experiments were performed with a universal testing machine (Walter + Bai AG, Switzerland with a 50kN load cell) with load accuracy of $\pm 0.5\%$ at a constant deformation rate of 2 mm/min. The deformation was monitored by a two-dimension (2D) Digital Image Correlation (DIC) system. An optical microscope (Keyence VHX-5000) was used to collect side cross-sectional pictures for thickness measurements.

2.2. DCB joint fabrication and test method

Cross-ply laminates $[90/0]_{7S}$ with an average total thickness of ca. 9.5 mm, fabricated under the same conditions as the tensile specimens discussed in the previous paragraph were used for the adherends. No special surface pre-treatment was applied, except the protection with the peel-ply that was only removed before the joint fabrication. Controlling the thickness of the adhesive through the use of spacers proved to be challenging. The intuitive fabrication method involves the placement of spacers to establish the thickness, filling the resulting cavity with adhesive, and flattening the surface by removing any excess material with a scraper. Nevertheless, the scraper could remove more adhesive than desired because of its high viscosity, hindering the quality of contact between the top adherend and the adhesive. In light of this, the establishment of good contact between top adherend and adhesive layer was achieved by using additional spacers that were inserted and removed during the process, as shown in Fig. 1. In this method (Method

I), adhesive material was added in two stages with excess adhesive being removed after each stage. The first stage consisted in pouring the adhesive into the cavity formed by setting the first spacers. Then, a defined length of Polytetrafluoroethylene sheet was positioned to define the pre-crack. In the second stage, the cavity that is generated by positioning the second and third spacers was once more filled with adhesive. The excess adhesive was removed with the third spacers still placed. Finally, these additional third spacers were removed and the top adherend and metal mold were placed on the top in sequence. The curing process followed the datasheet recommendations, i.e. 70 °C for four hours. After curing, the joints were cut with water jet and polished, and piano hinges were attached to the specimens. White background and black pattern were sprayed on the side surface of the joints for DIC technique.

However, many voids were observed from the side view of the specimens and by post-mortem observations of the failure surfaces. These affect the behavior of the thick adhesive joints. To address this issue, a second method (Method II) was proposed to control the void content, as illustrated in Fig. 2a. Round spacers were attached to the bottom adherends prior to mixing the SP830 adhesive. Proper amount of hand-mixed adhesive was then poured inside the cavity. After placing the top adherend, sufficient pressure was applied to squeeze out excess adhesive and minimize the amount of voids. After the adhesive solidified, the specimen was demolded and cured at 70 °C for four hours. The pre-crack was cut using a band saw and then the final 5 mm cut was performed using a diamond wire saw with a 0.125 mm diameter wire. Following the curing process, the joints were cut and polished, and piano hinges were fixed to the specimens. To facilitate DIC analysis, a white background with a black pattern was sprayed onto the lateral surface of the joints, and a ruler was stamped on the specimen surface close to the crack plane. The crack length was thus measured by image analysis of the DIC pictures recorded during each test, with the aid of the ruler.

Additionally, to further guide the crack propagation direction, some specimens produced with the second method were grooved on both sides, as shown in Fig. 2c. Removed adhesive material has a right-triangle cross-section on both sides with a 45°-tilted universal milling machine Schaublin 53 (accuracy 0.02 mm) equipped with a 20 mm

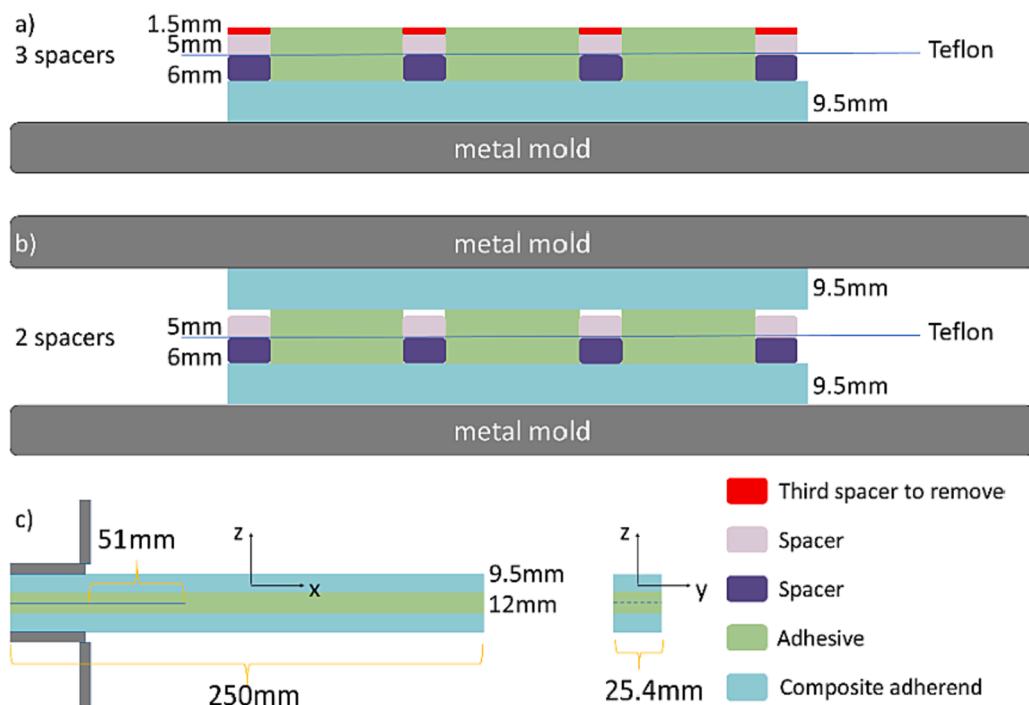


Fig. 1. Illustration of the joint manufacturing method I by adding and removing additional spacers: a) before removing the additional spacers; b) removing the additional spacers and putting the top adherend and mold; c) sample illustration before tests with piano hinges.

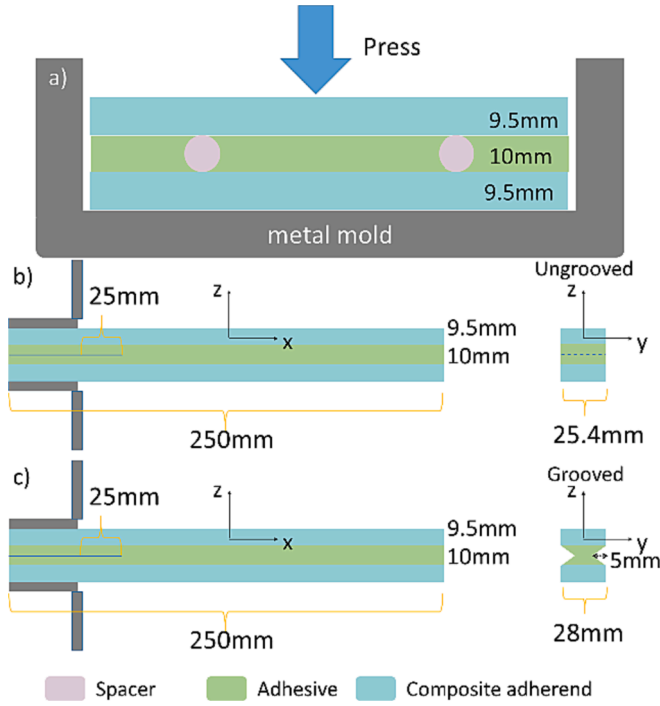


Fig. 2. Illustration of the joint manufacturing method II by applying enough pressure to control the void content: a) joint manufacturing under press; b) ungrooved specimen; c) grooved specimen.

diameter cylindrical cutter (code 862, FRAISA SA). Three classes of joints were thus manufactured with different void contents, i.e. low, medium, and high void content.

Joints made with Method I and ungrooved joints made with Method II were tested with the same machine used for the adhesive tensile test with 2D DIC technique. The speed was 2 mm/min. Grooved joints made with Method II were tested with an MTS Landmark servo-hydraulic testing machine, calibrated to 5 kN load capacity with three-dimensional (3D) DIC technique. The DCB set-up is shown in Fig. 3. Two test speeds were used, 1 mm/min and 0.24 mm/min. The test matrix including test conditions is given in Table 1. The number-of-specimen column shows the ratio of validated data-processed joints to the total number of fabricated joints subjected to testing. In the results section, discussion is provided for a single representative result within each group, while the other results are presented in the [supplementary information](#).

To compare the effects of two fabrication methods resulting in different void content, UN1 and UN2 specimens were employed. Furthermore, GN2 and GL2-L specimens were utilized to examine the influence of side grooved shape and loading rate on crack path selection, while GL2-M and GL2-H specimens were tested to investigate the impact of void content.

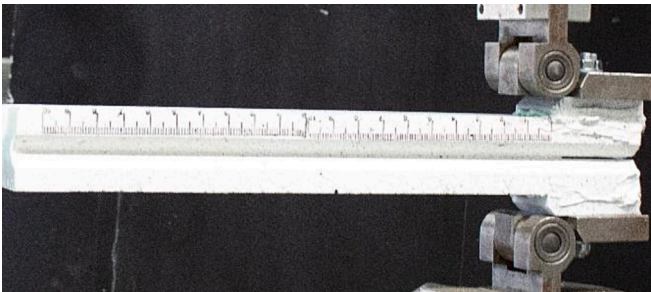


Fig. 3. The thick DCB experimental set-up.

GN2 and GL2-L joints with the lowest void content were manufactured by applying pressure on the adhesive (without level control usually performed by spacers), with the consequence that thickness control was not perfect. Due to the difficulty of manufacturing and the cutting procedure error, only one specimen for each type was tested. Joints with medium and high void content have a uniform thickness. After the DCB tests, the void distribution of joints was assessed by conducting 3D X-ray tomography (RX Solutions Ultratom) on the stable crack propagation area. AVIZO software was used for epoxy and void segmentation and void distribution reconstruction.

2.3. Data reduction method

Considering the SBT method, the contribution of adhesive layer to flexural rigidity is omitted for thin adhesive joint tests, whereas it is important for thick adhesive joints. The calculation of flexural rigidity is based on the geometry of the arm, as shown in Fig. 4. The first step is to calculate the neutral axis position (\bar{z}) and then calculate flexural rigidity (EI). SBT method can be inaccurate, since it does not consider the shear deflection, root rotation, and plastic zone deformation.

$$\bar{z} = \frac{\frac{E_c}{E_a} A_c \bar{z}_c + A_a \bar{z}_a}{\frac{E_c}{E_a} A_c + A_a} \quad (1)$$

$$EI = E_c I_c + E_c A_c |\bar{z}_c - \bar{z}|^2 + E_a I_a + E_a A_a |\bar{z}_a - \bar{z}|^2 \quad (2)$$

$$G_{SBT} = \frac{P^2}{2b} \frac{dC}{da} = \frac{P^2 a^2}{b \times EI} \quad (3)$$

$$G_{CBT} = \frac{3P\delta F}{2b(a + |\Delta|)} \quad (4)$$

$$G_{ECM} = \frac{nP\delta F}{2ba} \quad (5)$$

Here, the corner marker c and a are composite adherend and adhesive separately. E is the elastic modulus, A is the cross-section area and z the position of the center of gravity. P is the load, a is the crack length and b is the crack width. G is the strain energy release rate. Since CBT and ECM calculation considers the compliance of the whole beam, including the adhesive layer contribution, the adaption is not needed. Equation (4) and (5) are described in [38], where $|\Delta|$ is the crack length correction and F is the large-displacement correction factor. If the crack path changes from the middle of the adhesive to the adherend, the neutral axis position shifts leading to mixed-mode fracture. Consequently, these equations hold validity solely in cases where crack propagation takes place exclusively within the adhesive layer.

The load-displacement (P- δ) prediction curves are calculated based on SBT and CBT. The curves are separated into two parts. The initiation curve before crack propagation is expected to have a linear relation. The other one is the propagation curve, where the crack length is expressed in terms of compliance and substituted into G calculation equation. a_0 is the pre-crack length. \bar{G} is the average SERR value, and depending on the different groups the data used for the average G calculation is not the same, as detailed in each section.

$$P = \frac{3\delta \times EI}{2a_0^3} \quad (6)$$

$$P = \sqrt[4]{\frac{4\bar{G}^3 b^3 \times EI}{9\delta^2}} \quad (7)$$

Table 1
DCB test matrix.

Name	Fabrication method	Size	Grooved/ ungrooved	DIC technique	Speed	Void content	Number of specimens
UN1	Method I	Composite adherend width 25.4 mm; Adhesive layer thickness 12 mm	Ungrooved	2D	2 mm/min	High void content	4/4
UN2	Method II	Composite adherend width 25.4 mm; Adhesive layer thickness 10 mm	Ungrooved	2D	2 mm/min	Low void content	2/4
GN2	Method II	Composite adherend width 28 mm; Adhesive layer thickness 10 mm	Grooved	3D	1 mm/min	Low void content	1/1
GL2-L	Method II	Composite adherend width 28 mm; Adhesive layer thickness 10 mm	Grooved	3D	0.24 mm/min	Low void content	1/1
GL2-M	Method II	Composite adherend width 28 mm; Adhesive layer thickness 10 mm	Grooved	3D	0.24 mm/min	Medium void content	4/4
GL2-H	Method II	Composite adherend width 28 mm; Adhesive layer thickness 10 mm	Grooved	3D	0.24 mm/min	High void content	4/4

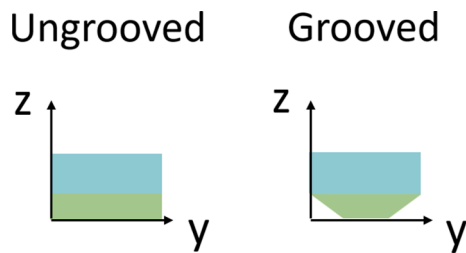


Fig. 4. Schematic of one arm for flexural rigidity calculation.

3. Results

3.1. Tensile behavior of the adhesive and adherend

The stress–strain curve of SP830 under tensile loading, as well as an example of the fracture surface, are illustrated in Fig. 5. The curve ends in fracture at around 42 MPa, indicative of its limited ability to undergo plastic deformation. Many voids with different sizes are evident from the fracture surface, which could be the reason for the large scatter in the results. A typical stress–strain curve for the composite laminate is presented in Fig. 6, showing a linear elastic behavior of the material until failure at a strain slightly lower than the failure strain of the epoxy adhesive. Side-view microscope photographs of the composite specimens are presented in Fig. 6b. Since a peel-ply was used to manufacture

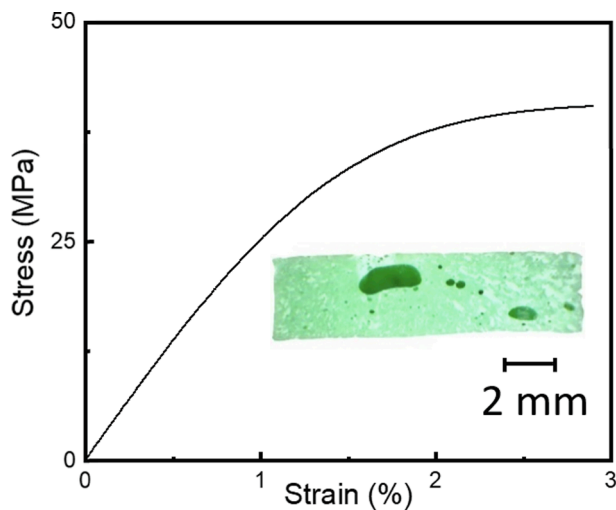


Fig. 5. SP830 tensile test result. strain–stress curve and corresponding fracture surface.

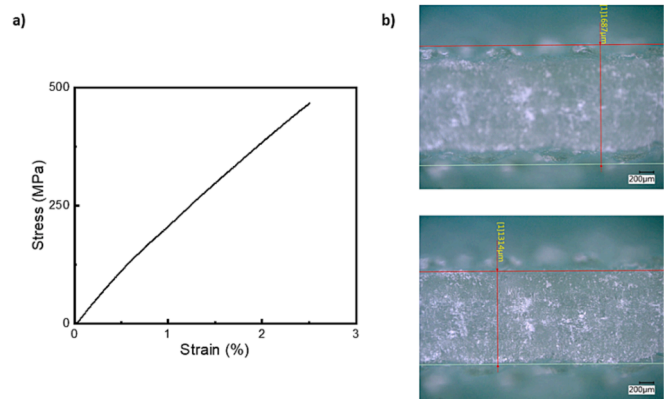


Fig. 6. Composite adherend tensile test result: a) strain–stress curve; b) microscope pictures before testing.

the composites, aiming at surface pattern creation and surface protection, both sides of the samples had a rough surface. Fig. 6b top indicates the total thickness measurement including roughness, which is 1.69 mm. The bottom picture in Fig. 6b shows the thickness without considering the rough matrix layer, which does not contribute much to the E-modulus. This value (1.31 mm) was chosen for the cross-section calculation. Table 2 displays the tensile test results of the adhesive and composite adherend.

3.2. DCB tests results

3.2.1. UN1 specimen

Fig. 7a presents the fracture surface of a thick DCB joint with many visible voids. Four distinct zones can be observed on the failure surface. The pre-crack region is on the left with the inserted Teflon sheet in the middle plane of the joint. Following this, there is a short area (light green) of ca. 1 cm where a stable crack propagated within the adhesive

Table 2
Tensile test results.

Adhesive (SP830) tensile test average results (5 samples)	Elastic modulus [GPa]	2.57 ± 0.12
	Ultimate Stress [MPa]	41.59 ± 1.15
	Strain at failure [%]	2.87 ± 0.31
Composite tensile test average results (4 samples)	Elastic modulus [GPa]	23.57 ± 1.13
	Ultimate Stress [MPa]	459.07 ± 8.09
	Strain at failure [%]	2.44 ± 0.05

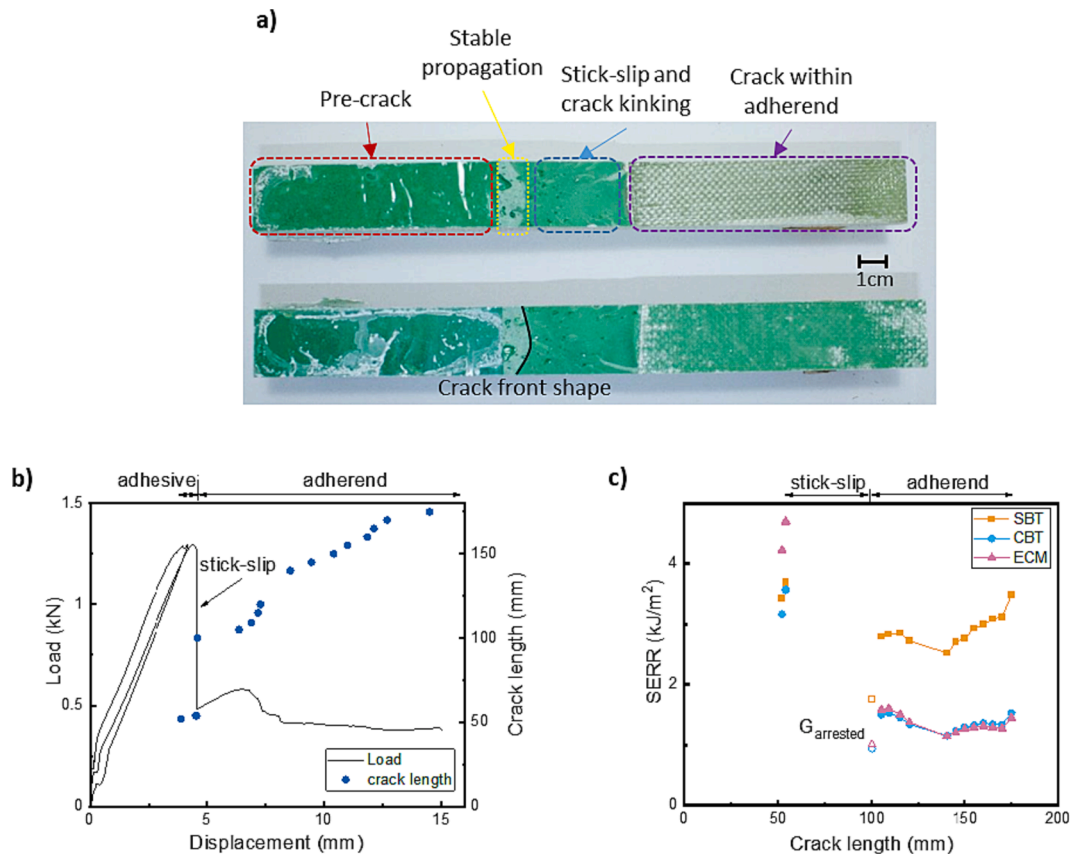


Fig. 7. Results of UN1 specimen: a) fracture surface after test and b) corresponding load–displacement curve c) corresponding SERR curves.

layer. After this length, the crack propagated fast (unstable crack shown in dark green) and kinked to the adherend after ca. 3 cm where it was arrested between the first and second layer of glass fabric. The fiber direction of the first layer is parallel to the y-axis (Fig. 2) and the second layer is parallel to the x-axis. As a result, the first layer was readily penetrated by the fracture. After being arrested, the crack propagation restarted in between these two layers. The crack front is slightly curved, as observed on the bottom of Fig. 7a. This creates a potential error in the SERR calculation which assumes a straight crack, as explained in [39], the influence is not large.

Fig. 7b summarizes the load–displacement curve and the crack length measurements. The stick–slip crack propagation is revealed by the vertical line in the curve, which is also visible from the crack length data. After this unstable propagation, the crack reached the adherend and the propagation restarted within the adherend. The max load is higher than 1.5 kN, which indicates a high initial crack propagation energy release rate.

SERR results are plotted in Fig. 7c. Since limited data was obtained for the adhesive propagation, the CBT and ECM calculations are based on the adherend propagation region, i.e. after the stick–slip crack propagation. Inspecting the adherend propagation, SBT results are observed to be higher than CBT and ECM, which can be attributed to the change of crack path that shifts from the adhesive to the adherend causing mixed-mode fracture. The neutral axis position is also shifting in this case, and therefore the calculated SERR results are not valid. Furthermore, the crack initiation also involves the formation of an arch-shaped crack and the crack propagation kinetic energy contribution. The crack measurement is also a big challenge since the result is really sensitive to the true crack length. When the crack propagation also involves stick–slip and crack kinking, the analysis is more difficult. Therefore, in the following sections, only the stable propagation region, which provides several SERR data points, will be utilized for

calculations. However, to provide a comprehensive understanding of the material behavior, the initiation and arrested SERR values of stick–slip propagation that occur after stable propagation and arrested within the adhesive layer will also be presented.

The results of the other three specimens are shown in the [supplementary information, Figs. S1 to S3](#), which show similar behavior.

3.2.2. UN2 specimen

Fig. 8a illustrates the fracture surface of a UN2 specimen after test. Similar to the results above, the fracture surface can be divided into four zones: pre-crack, stable adhesive propagation, stick–slip propagation and adherend propagation. Compared with Fig. 7a, the pre-crack region is shorter and fewer voids are observed. However, the trajectory of fracture propagation was similar. Both the stick–slip crack growth and the crack kinking occurred simultaneously. The stable and unstable propagation region can still be distinguished by the color of the fracture surface (light green and dark green). Eventually, the crack propagated within the adherend between the first and second layer of glass fabric until full separation.

The load–displacement curve is presented in Fig. 8b and SERR results of crack propagation within adherend are shown in Fig. 8c. The calculated SERR results are not valid because of the crack path deviation. Even though no visible large void was visible, the crack deviation occurred. As a consequence, grooved specimens were designed and tested to guide the crack propagation path.

The results of another specimen are shown in the [supplementary information, Fig. S4](#), which shows similar behavior.

3.2.3. GN2 specimen

The fracture surface is depicted in Fig. 9. A different pattern was observed in the middle part compared with the results shown above. Two light green regions (stable propagation) are separated by one dark

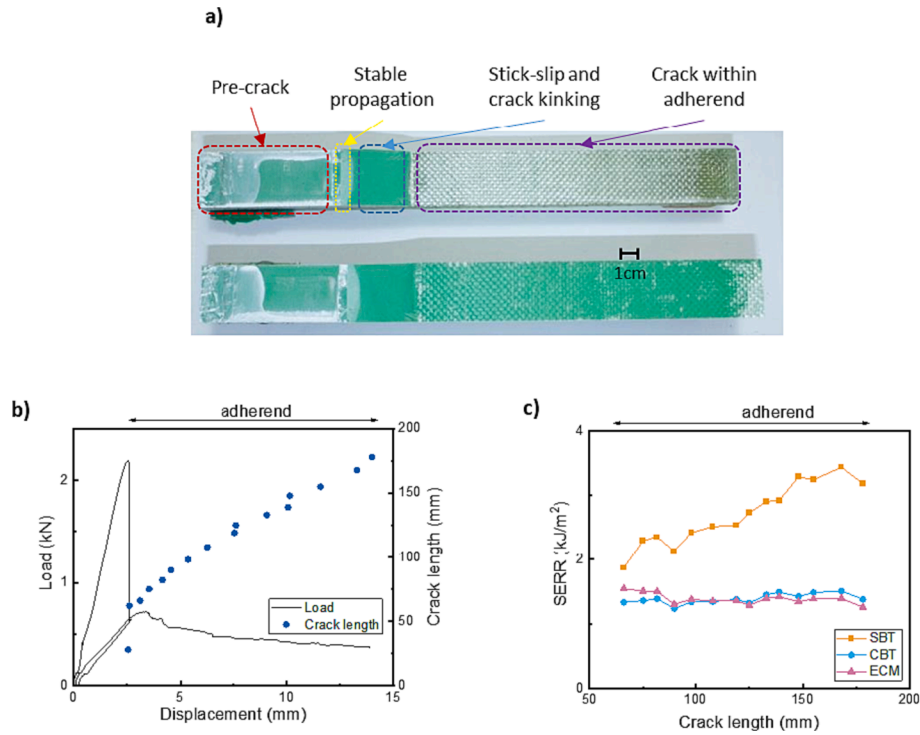


Fig. 8. Results of UN2 specimen: a) fracture surface after test b) corresponding load–displacement curve c) corresponding SERR curves.

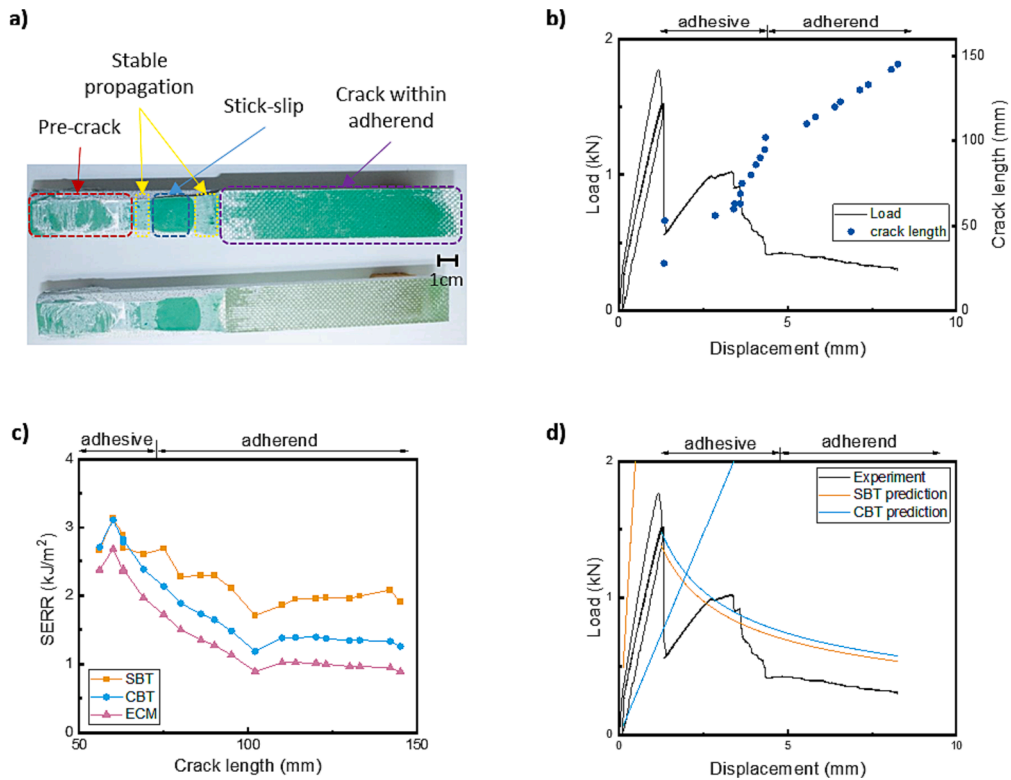


Fig. 9. Results of GN2: a) fracture surface after test b) corresponding load–displacement curve c) corresponding SERR curves d) prediction and experimental load–displacement curves.

green region (unstable propagation). The stick-slip and crack kinking did not happen simultaneously. For grooved specimens, the arrested crack position after stick-slip is still uncontrollable. If the crack is halted inside the grooved path, the crack could continue propagating straight.

Otherwise, crack kinking ensues. Concerning this sample, the crack tip already diverged from the middle plane when the crack was arrested after the stick-slip crack propagation. Therefore, when the crack propagation restarted the propagation tends to go towards the adherend

stably and it finally propagated between the first and second layers of glass fabric.

It is feasible to include adhesive propagation region into SERR calculation, although crack kinking occurred. The results are illustrated in Fig. 12c. The calculated SERR results are again not valid, especially when the crack propagates within the adherend. CBT and ECM parameters are calculated based on the stable crack propagation within the adhesive after the stick-slip and they are consistent with each other. The SERR values declines, since the crack propagated towards the adherend, and the cross-section area became larger than the one utilized for SERR calculation taken from the grooved middle plane path.

The SBT and CBT prediction curves are represented in Fig. 12d. Equation (6) and (7) were used for the derivation of the prediction curves. The displacement values are taken as the independent variable and the calculated load values are the dependent variable. The crack initiation region (equation (6)) is linear. However, the linear prediction curves and the experimental results diverge significantly. The crack propagation region (equation (7)) is predicted using average SERR values during stable propagation within the adhesive layer as one fixed

parameter (\bar{G}). In the following sections, this parameter will be adjusted to optimize its suitability for the specific situation being analyzed. The crack propagation region shows monotonically decreasing force with displacement. The CBT prediction is fitted to the tendency defined by two crack start points. The deviation after the restarting is deemed to originate from the crack path deflection. The SBT prediction is marginally lower than the other without considering the contribution of root rotation and plastic zone energy dissipation.

The arrested position after unstable propagation is unpredictable, so it is crucial to ensure the first stable propagation area is sufficiently long for analysis and SERR calculation. To further control the crack propagation, grooved DCB joints were tested with low cross-head speed.

3.2.4. GL2-L specimen

Fig. 10 shows the joint test results with low void content. As discussed, its thickness varies from 10 mm at the beginning to 14 mm at the end of the sample. Fig. 10a depicts the fracture surface, which exhibits pre-crack region, stable propagation, and fast arm separation regions. Stick-slip crack propagation and crack kinking only occurred when the

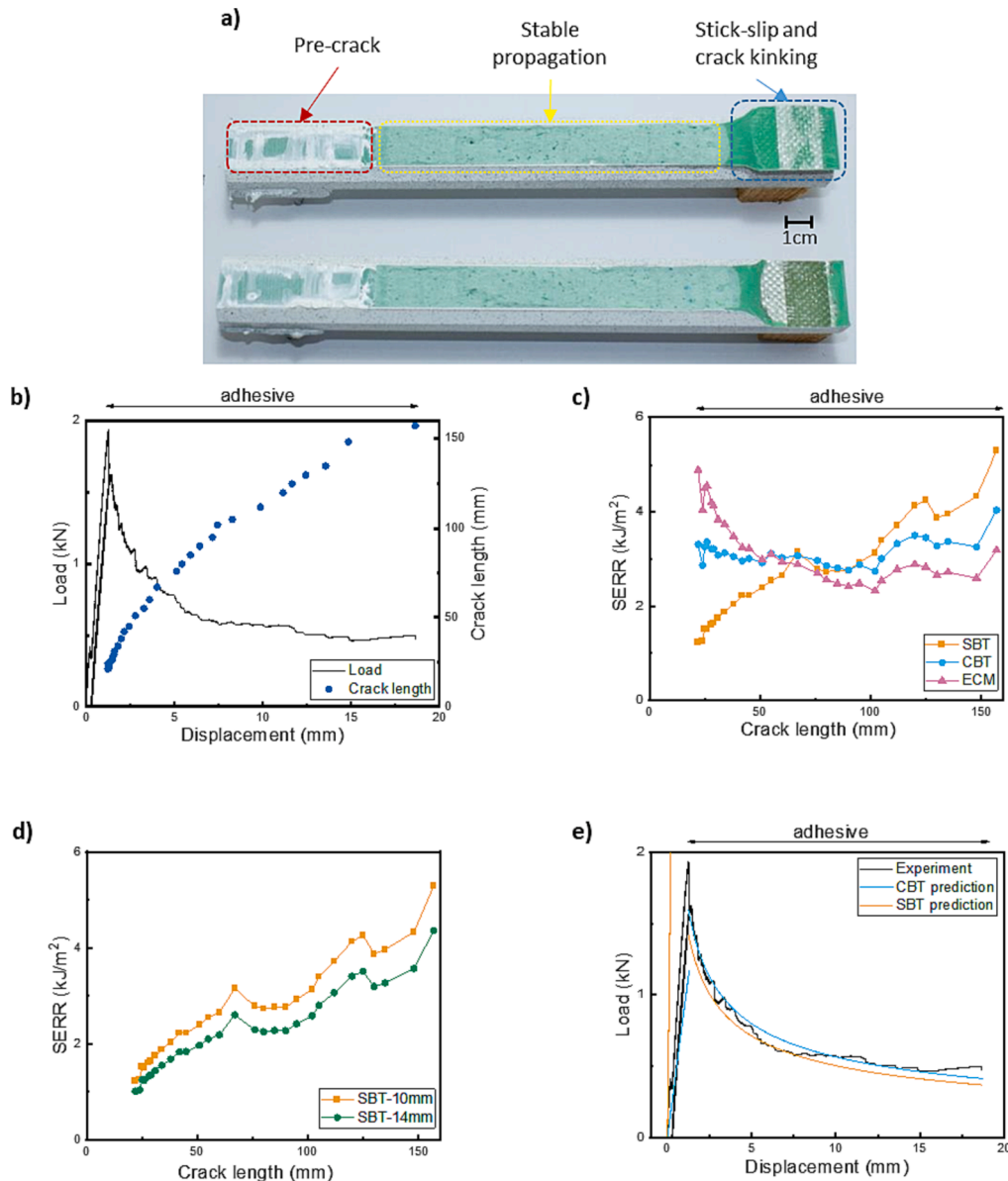


Fig. 10. Results of GL2-L specimen: a) fracture surface after test b) corresponding load-displacement curve c) corresponding SERR curves d) SBT SERR curves with two different adhesive layer thickness e) prediction and experimental load-displacement curves.

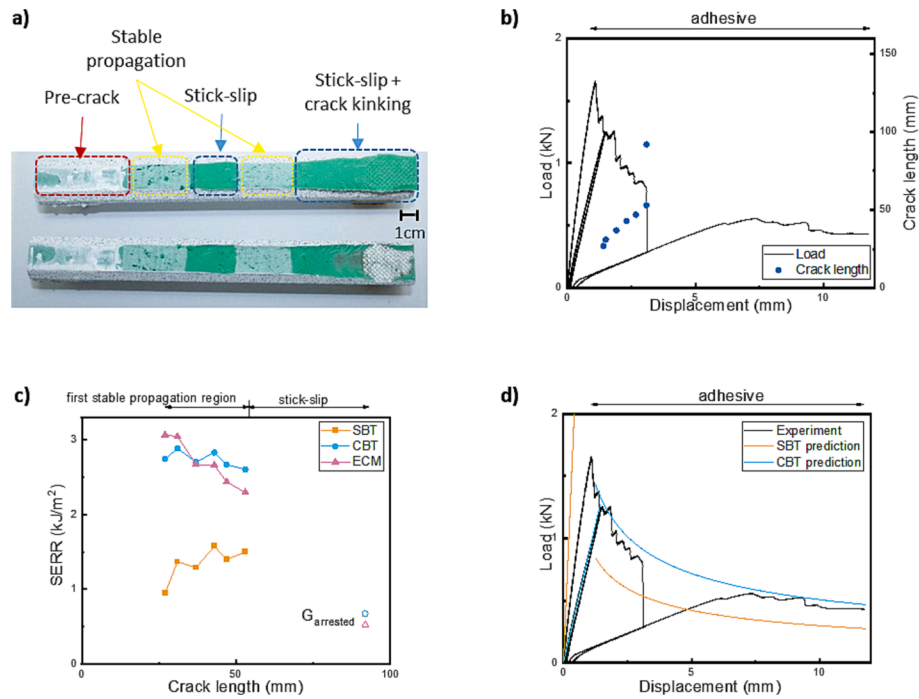


Fig. 11. Results of GL2-M specimens: a) fracture surface after test, b) corresponding load–displacement curve, c) corresponding SERR curves, d) prediction and experimental load–displacement curves.

two arms were completely separated. The long middle region with light green color corresponds to the stable propagation. The load–displacement data is plotted in Fig. 10b.

Fig. 10c illustrates the SERR curves derived by SBT, CBT, and ECM methods. The SBT curve shows an increasing trend, while the CBT results converge to the mean value of 3.16 kJ/m^2 . In the contrast, the ECM values tend to decrease after the crack starts to propagate. The increase in the SERR values at the final stage could be attributed to the thickness variation. The impact of thickness on SERR calculation is illustrated in Fig. 13c, where SBT results with 10 mm and 14 mm uniform thickness assumptions are calculated and compared. Around 20 % decrease is observed when the thickness increases by 4 mm. Shivakumar et al. [40] conducted sandwich DCB debonding tests to measure interfacial SERR values. They concluded that the ECM and CBT methods are valid when the crack length is smaller than half of the specimen length, which could be another source of the increasing SERR values at the end section.

The SBT and CBT prediction curves are depicted in Fig. 12d as dashed lines with both initial linear region and crack propagation region. The propagation curves were predicted based on the average SERR values separately. The CBT curve slightly differs from the experimental results, which can be explained by the fracture surface roughness, arch-shaped crack, and the distribution of small voids and flaws. Larger offset between SBT prediction and experimental curves is visible. However, the initial linear prediction does differ much from the experimental data.

Another two groups of joints with more and the most void contents were also manufactured by controlling the quantity of the adhesive. They were used to study the influence of void content on the fracture behavior of thick adhesive joints.

3.2.5. GL2-M specimen

Joints with medium void content (GL2-M specimens) have a uniform thickness. Inspecting the fracture surface (Fig. 11a), many voids are observed and light green color and dark green color regions stagger, indicating that stick–slip took place several times. It is obvious that there is a void at the boundary of the first stick–slip that corresponds to the vertical line in the load–displacement curve (Fig. 11b). After the first

stick–slip crack propagation, the crack was arrested at the middle plane, so the crack could still propagate without path deviation. In the end, the unstable propagation went along the interface and broke the joint. Data before the first stick–slip was used for the calculation. SERR curves are shown in Fig. 14c, even though limited data is obtained before the first stick–slip, the curve tendency is still similar to the previous results with low void content. SBT results are still much smaller than CBT and ECM. Increasing and decreasing trends are observed for SBT and ECM separately.

Then, the average values (without considering the arrested SERR value) were used for prediction curve calculation, which is plotted as dashed lines and compared with the experimental data in Fig. 11d. CBT propagation prediction and experimental curves are in agreement with each other, even though unstable crack propagation occurred. The experimental curve restored and converged towards the prediction curve after the first stick–slip crack propagation. Therefore, using the results calculated from the first stable propagation region can properly predict the loading curve of the second stable propagation region. It is inferred that the stick–slip crack propagation does not affect the validation of the calculation theory. The joint with medium void content is still suitable for DCB static test.

The results of the other three specimens are shown in the supplementary information, Figs. S5 to S7, which show similar behavior. As explained, once the stick–slip propagation occurred, the arrested position is unpredictable, so the fracture behavior varies from case to case.

3.2.6. GL2-H specimen

The fracture surface of joints with high void content is dominated by voids. Depending on the void size and distribution, a different fracture behavior can be observed. When the crack tip encounters large voids, stick–slip crack propagation takes place, as shown in Fig. 12a. Fig. 12b depicts the other possibility, if the voids are not too large with an adequate shape, stable propagation can be achieved. In addition, the crack kinking direction can be inversed, which is obvious in Fig. 12b. Fracture tends to choose the crack path consuming less energy that contains voids, since the adhesive is already separated by the voids. The

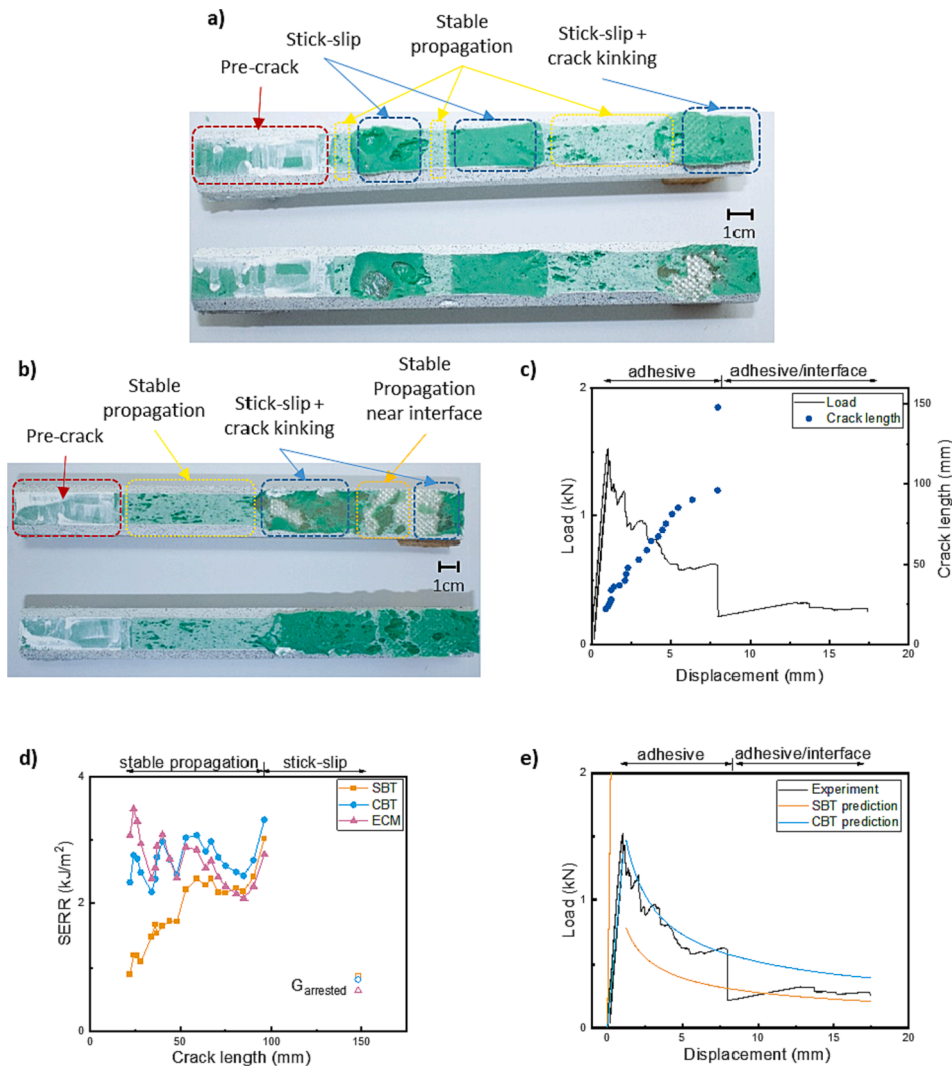


Fig. 12. Results of GL2-H specimens: a) one fracture surface after test, b) another fracture surface after test, c) corresponding load–displacement curve, d) corresponding SERR curves, e) prediction and experimental load–displacement curves.

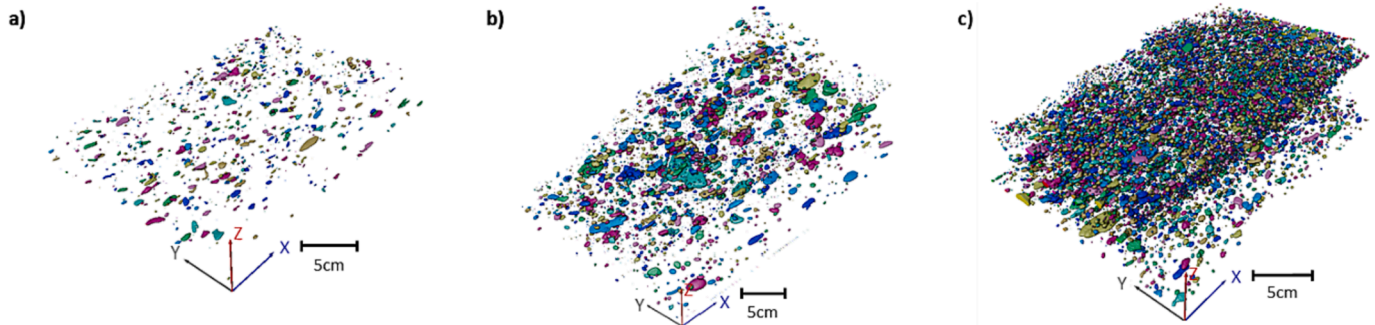


Fig. 13. X-ray tomography of void distribution of three samples shown above after static test.

crack finally went back to the adhesive layer from the interface to the adhesive. In these two cases, the crack never went through the first glass fabric, either remaining at the interface or switching between the interface and the adhesive.

Since the second sample (Fig. 12b) has sufficient stable propagation length, the related load–displacement curve, SERR calculation and prediction curves are plotted in Fig. 12, using the data obtained before the first stick–slip. The CBT data is consistent with ECM data, while the

progressive increased SBT data differs from the others. The curve depicting large voids fluctuates more compared with low void content results, and the valley values can be down to 2.3 kJ/m² between peaks close to the value found in the low void content case, which is around 3.1 kJ/m².

Because of the fluctuating SERR results, the prediction curve is calculated with the first peak SERR value, assuming that peak values are not influenced by voids. Comparing the CBT prediction and

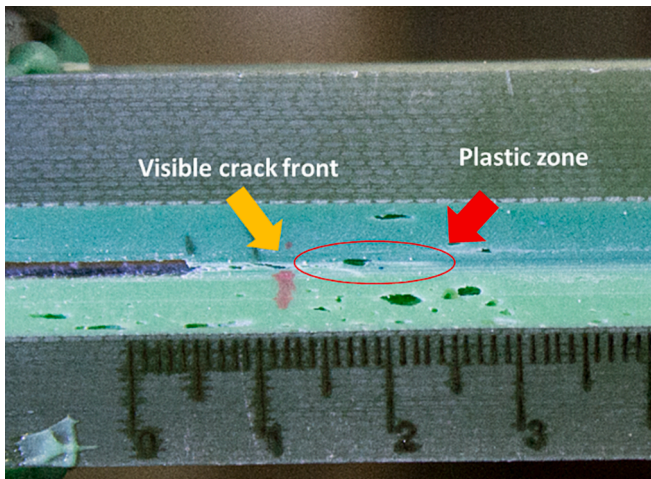


Fig. 14. Picture of joint crack measurement issue.

experimental data, the prediction curve links the peak values of the experimental data, which accords with the calculation assumption. Nevertheless, SBT prediction is much lower than the experimental curve.

The results of the other three specimens are shown in the supplementary information, Figs. S8 to S10, which show similar behavior. As explained, once the stick-slip propagation occurred, the arrested position is unpredictable, so the fracture behavior varies from case to case.

4. Discussion

4.1. Grooved geometry

The side-grooved shape could guide the crack propagation within the middle plane, since the grooved plane has the smallest surface area, so ideally the crack propagation consumes the lowest energy by selecting the grooved path without considering the voids. Other research has also highlighted the fact that the propagation path consuming less energy is preferable during the tests [41]. However, the actual situation is more complicated, so loading speed and void content are also critical factors that affect the crack propagation path.

4.2. Loading speed

The loading rate influence is related to material properties. First, increasing the loading rate could lead to a ductile-brittle transition, which might allow the unstable propagation to take place. Second, the large differential between initiation and propagation fracture toughness could lead to unstable propagation [21]. The comparison between G2N and G2L-L results demonstrates that in order to maintain stable propagation of thick adhesive joints, low speed is preferred.

The crack propagation kinetic energy is not negligible, and also related to the loading rate [42]. By comparing stick-slip crack propagation at two different cross-head speeds, it can be seen that a crack with a fast speed can easily penetrate the first layer of the fabric, while it is difficult for a crack with a slow speed to penetrate it. To valid the slow speed (0.24 mm/min) DCB propagation results, a creep test was also conducted with a GL2-M specimen. After 5 mm crack propagation, the creep test was employed at 1.5 kN for 30 mins. During the test, no obvious crack propagation was observed.

4.3. Void content

The effect of the void content is clearly noticeable, especially by analyzing the results of GL2-L, GL2-M, and GL2-H specimens. To further

unveil the relation between the void content and the fracture behavior, the void distribution is demonstrated in Fig. 13. Since the adhesive has a yield stress (adhesive cannot flow without external force), the adhesive was applied to cover the whole surface of the cavity using a scraper, resulting in that the direction of the voids follows the application direction. This proves that applying the adhesive is a critical step where many voids are created. It is recommended to add the adhesive layer upon layer and to degas the adhesive several times to avoid large voids.

Void distribution is depicted in Fig. 13 and the corresponding information is shown in Table 3. Only voids inside the fractured samples were included in the analysis (the voids on the edge and fracture surface are excluded). Large voids emerge more frequently in high void content joints. It is obvious that void volume percent and the distribution of extremely large voids dominate the final results. Similar to the side-grooved shape, the crack path over large voids consumes less energy, whereas when the voids are too large, this lowest energy propagation path is no longer the grooved path and replaced by the path with large voids. Moreover, the existence of voids will influence the stress state ahead of the crack tip, so the crack has a high possibility to deviate from the middle plane of the joints. The combination of the two aforementioned reasons could lead to crack kinking. From our observation, depending on the void distribution, joints with void volume percent higher than 4 % might experience crack kinking anytime throughout the test. Controlling the void volume lower than 2 % could thus help the fracture mechanics investigation.

Large dimension voids are one main cause of the stick-slip crack propagation. It has already been proven that when the crack encounters voids, the plastic zone size is influenced and the crack growth rate changes [42]. Besides this, the SERR value suddenly drastically decreases since the surface area decreases, so the stable propagation cannot be maintained, some energy was dissipated into kinetic energy, triggering stick-slip crack propagation.

By observing the SERR curves in Figs. 10-12, despite the fact that limited data is shown for the joint with medium void content, stable tendencies are still observed for the classes of small and medium void contents. As for the joint with high void content, the apparent SERR curve is more erratic. A possible explanation for this discrepancy is that the SERR calculation assumes a constant surface area, whereas the surface area decreases when voids are present. In addition, the average values of the SERR do not vary much among the three classes. It can thus be suggested that void is one main source of stick-slip and crack kinking, while it will not influence much on the SERR calculation. For joints with small or medium void content, grooved geometry can guide the crack propagation direction, providing sufficient data for the SERR calculation.

4.4. SERR calculation methods and prediction

For SERR calculation, UN1, UN2 specimens show higher SERR values using the SBT method compared with the ECM and CBT methods. Normally, the SBT method results in the lowest SERR values as it does not consider any plastic zone and root rotation. The crack kinking also leads to the neutral axis shifting. In our cases, SERR values are calculated based on the adherend propagation section, where the mixing of mode I and II can be observed and the plastic zone size and root rotation influence are different compared to pure mode I so the inversed trend

Table 3

Void content in three grooved samples shown above.

Sample type name	Number of voids larger than 1 mm ³	Number of voids larger than 0.1 mm ³	Void volume percentage	Largest voids volume
GL2-L	0	33	0.36 %	0.75 mm ³
GL2-M	24	232	2.19 %	10.32 mm ³
GL2-H	20	587	4.13 %	9.87 mm ³

was observed. When the crack propagated within the adhesive layer, SBT results are much lower than the other two. ECM data is similar to CBT one, while it is more scattered, which is also observed in sandwich DCB debonding tests [40,43].

The average CBT SERR values for joints made with composite adherend and 10 mm thick SP830 adhesive layer is around 3.16 kJ/m². SERR value can also be estimated from fracture toughness by using equation (8). Fracture toughness (K_{IC}) is determined from the single-edge-notched-bend tests, obtained from [44] and Poisson's ratio is assumed to be 0.38. The resulting value is about 2.6 kJ/m², which slightly differs from the joint test result.

$$G = \frac{K^2}{E/(1 - \nu^2)} \quad (8)$$

As for the prediction curves, the initial linear curve calculation shows large difference from the experimental results, whereas the crack propagation CBT curves are consistent with experimental curves. The reason is complicated. First, the crack measurement is taken from the DIC pictures from one side of the joint, which is not accurate. The painting itself also hinders the measurement whose breaks may be asynchronous with the joint. Fig. 14 shows one example of joints under loading without paint. There is a region ahead of the crack tip that changed into white color, which is the plastic zone. This is consistent with the DIC analysis. There is a region with large deformation (>3%) ahead of the visible crack tip. Besides these, the residual stress from the curing process is also an influencing factor. Thus, the initial linear prediction exhibits a significant deviation. Nevertheless, all these results lead to the mismatch between theory and the experiments whose influence is independent of the crack length, so they can be included in the CBT and ECM SERR calculations and CBT crack propagation prediction, but not in SBT. In conclusion, it is inferred that CBT calculation is valid for thick adhesive DCB joint tests.

5. Conclusions

Thick-DCB-joint static tests were conducted in this research with varying geometry, cross-head speed, and void content to study their influence on the fracture behavior. Grooved specimens with low void content and low testing speed are most adequate for SP830 and composite adherend joint testing. CBT calculation is a proper data reduction method, even though thickness control and crack length measurement are to be considered.

The grooved geometry is used for the first time for thick DCB joint investigation. The findings of this study suggest that using grooved geometry can help guide the crack propagation path and simplify the data reduction process by using the commonly accepted SERR calculation methods, such as CBT and ECM.

The void content within the adhesive layer is an important influencing factor. This research has provided a deeper insight into the void-dominating fracture behavior. It is obvious that large voids ahead of the crack tip can lead to stick-slip crack propagation. After, the joint behavior is unpredictable. Ideally, low void content is beneficial for stable crack propagation without crack kinking. Joints with 2 % volume percent voids can still be tested with sufficient stable crack propagation length, while high void content is not recommended, since it can result in fluctuating SERR curve or more complicated behavior. Fracture will prefer to choose the path with voids, which consumes less energy.

Nevertheless, because of the difficulty of joint manufacturing, especially for the low void content adhesive joint, the results are constrained by the limited sample size. Generalization of the conclusions to other systems and manufacturing techniques of the samples would require a larger set of experimental tests.

CRedit authorship contribution statement

Jialiang Fan: Investigation, Methodology, Validation, Data curation, Writing – original draft. **Anastasios P. Vassilopoulos:** Conceptualization, Funding acquisition, Methodology, Supervision, Writing – review & editing. **Veronique Michaud:** Conceptualization, Funding acquisition, Project administration, Supervision, Writing – review & editing.

Declaration of Competing Interest

The authors declare that they have no known competing financial interests or personal relationships that could have appeared to influence the work reported in this paper.

Data availability

Links to Zenodo repository provided at the end of the manuscript.

Acknowledgements

The authors acknowledge funding under the Lead Agency scheme from the Research Foundation - Flanders (FWO Vlaanderen) through the project grant G031020N and the Swiss National Science Foundation (SNF) through the project grant 200021E_189444/1 with the title “Combined numerical and experimental approach for the development, testing and analysis of thick adhesive joints in large wind turbine blades”. The authors also acknowledge the experimental assistance provided by the technical team of the structural engineering experimental platform (GIS-ENAC at the Ecole Polytechnique Fédérale de Lausanne (EPFL), Switzerland), and Interdisciplinary Platform for X-ray micro-tomography (ENAC-PIXE). The authors also acknowledge Sika Technology AG for providing materials and support.

Data availability statement

The raw and analyzed data are uploaded in the Zenodo Repository, as follows:

[10.5281/zenodo.8366685](https://zenodo.org/record/8366685).
[10.5281/zenodo.8367180](https://zenodo.org/record/8367180).
[10.5281/zenodo.8367957](https://zenodo.org/record/8367957).
[10.5281/zenodo.8369129](https://zenodo.org/record/8369129).
[10.5281/zenodo.8369221](https://zenodo.org/record/8369221).
[10.5281/zenodo.8369406](https://zenodo.org/record/8369406).

Appendix A. Supplementary material

Supplementary data to this article can be found online at <https://doi.org/10.1016/j.compstruct.2023.117705>.

References

- [1] Wind Electricity – Analysis. IEA n.d. <https://www.iea.org/reports/wind-electricity> (accessed December 4, 2022).
- [2] Wind Turbines: the Bigger, the Better. EnergyGov n.d. <https://www.energy.gov/eere/articles/wind-turbines-bigger-better> (accessed December 4, 2022).
- [3] Memija A. 123-Metre Wind Turbine Blade Rolls Out in China. accessed December 4, 2022 Offshore Wind 2022. <https://www.offshorewind.biz/2022/09/07/123-metre-wind-turbine-blade-rolls-out-in-china/>.
- [4] Ataya S, Ahmed MMZ. Damages of wind turbine blade trailing edge: Forms, location, and root causes. Eng Fail Anal 2013;35:480–8. <https://doi.org/10.1016/j.engfailanal.2013.05.011>.
- [5] Mishnaevsky L. Root Causes and Mechanisms of Failure of Wind Turbine Blades: Overview. Materials 2022;15:2959. <https://doi.org/10.3390/ma15092959>.
- [6] Haselbach PU, Eder MA, Belloni F. A comprehensive investigation of trailing edge damage in a wind turbine rotor blade. Wind Energy 2016;19:1871–88. <https://doi.org/10.1002/we.1956>.
- [7] Lopes Fernandes R, Budzik MK, Benedictus R, Teixeira de Freitas S. Multi-material adhesive joints with thick bond-lines: Crack onset and crack deflection. Compos Struct 2021;266:113687. <https://doi.org/10.1016/j.compstruct.2021.113687>.

- [8] Bautista Villamil AA, Casas-Rodríguez JP, Porras Holguín A, Silva BM. Mode I Crack Propagation Experimental Analysis of Adhesive Bonded Joints Comprising Glass Fibre Composite Material under Impact and Constant Amplitude Fatigue Loading. *Materials* 2021;14:4380. <https://doi.org/10.3390/ma14164380>.
- [9] Saleh MN, Budzik MK, Saeedifar M, Zarouchas D, Teixeira De Freitas S. On the influence of the adhesive and the adherend ductility on mode I fracture characterization of thick adhesively-bonded joints. *Int J Adhes Adhes* 2022;115: 103123. <https://doi.org/10.1016/j.ijadhadh.2022.103123>.
- [10] Rosendahl PL, Staudt Y, Odenbreit C, Schneider J, Becker W. Measuring mode I fracture properties of thick-layered structural silicone sealants. *Int J Adhes Adhes* 2019;91:64–71. <https://doi.org/10.1016/j.ijadhadh.2019.02.012>.
- [11] Shahverdi M, Vassilopoulos AP, Keller T. Mixed-Mode I/II fracture behavior of asymmetric adhesively-bonded pultruded composite joints. *Eng Fract Mech* 2014; 115:43–59. <https://doi.org/10.1016/j.engfractmech.2013.11.014>.
- [12] Shahverdi M, Vassilopoulos AP, Keller T. Experimental investigation of R-ratio effects on fatigue crack growth of adhesively-bonded pultruded GFRP DCB joints under CA loading. *Compos A Appl Sci Manuf* 2012;43:1689–97. <https://doi.org/10.1016/j.compositesa.2011.10.018>.
- [13] Shahverdi M, Vassilopoulos AP, Keller T. Modeling effects of asymmetry and fiber bridging on Mode I fracture behavior of bonded pultruded composite joints. *Eng Fract Mech* 2013;99:335–48. <https://doi.org/10.1016/j.engfractmech.2013.02.001>.
- [14] Shahverdi M, Vassilopoulos AP, Keller T. A phenomenological analysis of Mode I fracture of adhesively-bonded pultruded GFRP joints. *Eng Fract Mech* 2011;78: 2161–73. <https://doi.org/10.1016/j.engfractmech.2011.04.007>.
- [15] Mostovoy S, Crosley P, Ripling E. Use of crack-line-loaded specimens for measuring plane-strain fracture toughness. *J Mater* 1967;2:661–.
- [16] Xu S, Dillard DA. Determining the impact resistance of electrically conductive adhesives using a falling wedge test. *IEEE Trans Compon Packag Technol* 2003;26: 554–62. <https://doi.org/10.1109/TCAPT.2003.817646>.
- [17] Andena L, Castellani L, Castiglioni A, Mendogni A, Rink M, Sacchetti F. Determination of environmental stress cracking resistance of polymers: Effects of loading history and testing configuration. *Eng Fract Mech* 2013;101:33–46. <https://doi.org/10.1016/j.engfractmech.2012.09.004>.
- [18] Labuz JF, Shah SP, Dowding CH. The fracture process zone in granite: evidence and effect. *Int J Rock Mech Min Sci Geomech Abstr* 1987;24:235–46. [https://doi.org/10.1016/0148-9062\(87\)90178-1](https://doi.org/10.1016/0148-9062(87)90178-1).
- [19] Johnson FA, Radon JC. Mechanical and metallurgical aspects of fracture behaviour of an Al-alloy. *Int J Fract* 1972;8:21–36. <https://doi.org/10.1007/BF00185195>.
- [20] Komatsu K, Sekiguchi Y, Ihara R, Tatsumi A, Sato C. Experimental investigation of an adhesive fracture energy measurement by preventing plastic deformation of substrates in a double cantilever beam test. *J Adhes* 2019;95:911–28. <https://doi.org/10.1080/00218464.2018.1451332>.
- [21] Guo S, Xia Y, Wei X, Zhou Q. Investigation on the stable and stick-slip crack propagation behaviors in double cantilever beam test. *J Adhes* 2020;96:1198–218. <https://doi.org/10.1080/00218464.2019.1568248>.
- [22] da Silva LFM, Öchsner A, Adams RD, editors. *Handbook of Adhesion Technology*. Cham: Springer International Publishing; 2018. 10.1007/978-3-319-55411-2.
- [23] Abdel-Monsef S, Renart J, Carreras L, Maimí P, Turon A. Effect of environmental conditioning on pure mode I fracture behaviour of adhesively bonded joints. *Theor Appl Fract Mech* 2020;110:102826. <https://doi.org/10.1016/j.tafmec.2020.102826>.
- [24] Blackman BRK, Kinloch AJ, Rodriguez-Sanchez FS, Teo WS. The effects of test rate on the fracture behaviour of adhesively bonded joints n.d.:7.
- [25] Schmandt C, Marzi S. Effect of crack opening velocity on fracture behavior of hyperelastic semi-structural adhesive joints subjected to mode I loading. *Procedia Struct Integrity* 2018;13:799–805. <https://doi.org/10.1016/j.prostr.2018.12.154>.
- [26] Park J-H, Choi J-H, Kweon J-H. Evaluating the strengths of thick aluminum-to-aluminum joints with different adhesive lengths and thicknesses. *Compos Struct* 2010;92:2226–35. <https://doi.org/10.1016/j.compstruct.2009.08.037>.
- [27] Chester RJ, Roberts JD. Void minimization in adhesive joints. *Int J Adhes Adhes* 1989;9:129–38. [https://doi.org/10.1016/0143-7496\(89\)90107-3](https://doi.org/10.1016/0143-7496(89)90107-3).
- [28] Zuo P, Vassilopoulos AP. Review of fatigue of bulk structural adhesives and thick adhesive joints. *Int Mater Rev* 2020;1–26. <https://doi.org/10.1080/09506608.2020.1845110>.
- [29] Griffin D, Malkin M. Lessons Learned from Recent Blade Failures: Primary Causes and Risk-Reducing Technologies. In: 49th AIAA Aerospace Sciences Meeting including the New Horizons Forum and Aerospace Exposition. Orlando, Florida: American Institute of Aeronautics and Astronautics; 2011. <https://doi.org/10.2514/6.2011-259>.
- [30] I. M. Foletti A, Sena Cruz J, Vassilopoulos AP. Fabrication and curing conditions effects on the fatigue behavior of a structural adhesive. *International Journal of Fatigue* 2020;139:105743. 10.1016/j.ijfatigue.2020.105743.
- [31] Lees DE, Hutchinson AR. Mechanical characteristics of some cold-cured structural adhesives. *Int J Adhes Adhes* 1992;12:197–205. [https://doi.org/10.1016/0143-7496\(92\)90054-Y](https://doi.org/10.1016/0143-7496(92)90054-Y).
- [32] Sayer F. *Sub-component testing for structural adhesive joint Assessment in Wind Turbine Rotor Blades*. Bremerhaven: Fraunhofer Verlag; 2020.
- [33] Sengab A, Talreja R. A numerical study of failure of an adhesive joint influenced by a void in the adhesive. *Compos Struct* 2016;156:165–70. <https://doi.org/10.1016/j.compstruct.2015.12.052>.
- [34] Shishesaz M, Tehrani S. The effects of circumferential voids or debonds on stress distribution in tubular adhesive joints under torsion. *J Adhes* 2020;96:1396–430. <https://doi.org/10.1080/00218464.2019.1605598>.
- [35] Rossettos JN, Lin P, Nayeb-Hashemi H. Comparison of the Effects of Debonds and Voids in Adhesive Joints. *J Eng Mater Technol* 1994;116:533–8. <https://doi.org/10.1115/1.2904324>.
- [36] ASTM D638. Test Method for Tensile Properties of Plastics. West Conshohocken (PA): ASTM International; 10.1520/D0638-14.
- [37] ASTM D3039M-17. Test Method for Tensile Properties of Polymer Matrix Composite Materials. ASTM International; 10.1520/D3039_D3039M-17.
- [38] Zhang Y, Vassilopoulos AP, Keller T. Mode I and II fracture behavior of adhesively-bonded pultruded composite joints. *Eng Fract Mech* 2010;77:128–43. <https://doi.org/10.1016/j.engfractmech.2009.09.015>.
- [39] Jiang Z, Wan S, Keller T, Fang Z, Vassilopoulos AP. Influence of curved delamination front on R-curve of DCB specimen. *Compos Struct* 2019;227:111311. <https://doi.org/10.1016/j.compstruct.2019.111311>.
- [40] Shivakumar K, Chen H, Smith SA. An Evaluation of Data Reduction Methods for Opening Mode Fracture Toughness of Sandwich Panels. *J Sandwich Struct Mater* 2005;7:77–90. <https://doi.org/10.1177/1099636205047085>.
- [41] Ranade SR, Guan Y, Moore RB, Dillard JG, Batra RC, Dillard DA. Characterizing fracture performance and the interaction of propagating cracks with locally weakened interfaces in adhesive joints. *Int J Adhes Adhes* 2018;82:196–205. <https://doi.org/10.1016/j.ijadhadh.2017.12.006>.
- [42] Heide-Jørgensen S, Budzik MK. Effects of bondline discontinuity during growth of interface cracks including stability and kinetic considerations. *J Mech Phys Solids* 2018;117:1–21. <https://doi.org/10.1016/j.jmps.2018.04.002>.
- [43] Carlsson LA, Kardomateas GA. *Structural and Failure Mechanics of Sandwich Composites*. vol. 121. Dordrecht: Springer Netherlands; 2011. 10.1007/978-1-4020-3225-7.
- [44] Fan J, Karami J, Kojouri A, Hemelrijck DV, Vassilopoulos A, Michaud V. Investigation of bulk adhesive material and thick adhesive joints for wind turbine applications 2022;vol. E:129–36.